Check for updates

View Article Online
View Journal

Journal of
Materials Chemistry A

Materials for energy and sustainability

Accepted Manuscript

This article can be cited before page numbers have been issued, to do this please use: I. Pinnock, Y. Fan, Y. Zhu, B. Narayan, T. Wang, I. P. Parkin and B. Deka Boruah, *J. Mater. Chem. A*, 2024, DOI: 10.1039/D4TA06572G.

This is an Accepted Manuscript, which has been through the Royal Society of Chemistry peer review process and has been accepted for publication.

Accepted Manuscripts are published online shortly after acceptance, before technical editing, formatting and proof reading. Using this free service, authors can make their results available to the community, in citable form, before we publish the edited article. We will replace this Accepted Manuscript with the edited and formatted Advance Article as soon as it is available.

You can find more information about Accepted Manuscripts in the Information for Authors.

Please note that technical editing may introduce minor changes to the text and/or graphics, which may alter content. The journal's standard Terms & Conditions and the Ethical guidelines still apply. In no event shall the Royal Society of Chemistry be held responsible for any errors or omissions in this Accepted Manuscript or any consequences arising from the use of any information it contains.

ROYAL SOCIETY OF CHEMISTRY

rsc.li/materials-a

View Article Online
DOI: 10.1039/D4TA06572G

Advancing High Capacity 3D VO_2(B) Cathodes for Improved Zinc-ion Battery Performance

Iman P. Pinnock,[1] Yujia Fan,[1] Yijia Zhu,[1] Bastola Narayan,[2] Tianlei Wang,[3] Ivan P Parkin,[3,*] Buddha Deka Boruah[1,*]

[1]Institute for Materials Discovery (IMD), University College London (UCL), London WC1E 7JE, UK

[2]Department of Mechanical Engineering, University of Bath, Bath, BA2 7AY, UK

[3]Department of Chemistry, University College London (UCL), London WC1H 0AJ, UK

Corresponding authors: Prof. Ivan P. Parkin: i.p.parkin@ucl.ac.uk

Dr. Buddha Deka Boruah: b.boruah@ucl.ac.uk

Open Access Article. Published on 22 November 2024. Downloaded on 11/26/2024 9:52:47 AM.
This article is licensed under a Creative Commons Attribution-NonCommercial 3.0 Unported Licence.

Journal of Materials Chemistry A Accepted Manuscript

View Article Online
DOI: 10.1039/D4TA06572G

Open Access Article. Published on 22 November 2024. Downloaded on 11/26/2024 9:52:47 AM.
This article is licensed under a Creative Commons Attribution-NonCommercial 3.0 Unported Licence.

Journal of Materials Chemistry A Accepted Manuscript

Abstract

Aqueous zinc-ion batteries (AZIBs) have gained attention for their intrinsic characteristics, driven by key advantages such as cost-effectiveness, widespread availability of zinc, and reduced environmental impact and make AZIBs a promising alternative to lithium-based batteries, with potential applications in mini-grid and mini off-grid energy systems. However, achieving high capacity is crucial for AZIBs, driving research focus towards developing advanced cathode materials. Vanadium dioxide (VO_2(B)) has emerged as a promising cathode material for AZIBs, owing to its large tunnel-like framework, which accommodates Zn^{2+} ions for enhanced capacity. The overall performance of cathode materials depends not only on their inherent properties, but also on synthesis methods, electrode processing techniques, and achieving ultra-high mass loading for 3D electrodes. In this study, we explore the optimization of VO_2(B) cathodes through refined synthesis approaches, various electrode processing methods, and the development of 3D electrodes with ultrahigh mass loading. As a result, we achieved significant improvements in specific capacity, from 310 mAh g^{-1} to 500 mAh g^{-1}, through parameter tuning. Additionally, our optimized cathodes demonstrated a stable capacity retention of 71.5% after 1000 cycles. We also developed ultra-high mass loading cathodes of 24 g cm^{-2}, achieving areal capacity of 4.6 mAh cm^{-2}, with a stability of 81.5% after 1000 cycles. This work provides a comprehensive approach to obtaining high-capacity cathodes, contributing to the advancement of reliable and high-performance AZIBs.

Keywords: Multiwave synthesis; hydrothermal synthesis; VO_2(B); vacuum drying; freeze drying; 3D cathodes.

View Article Online
DOI: 10.1039/D4TA06572G

Open Access Article. Published on 22 November 2024. Downloaded on 11/26/2024 9:52:47 AM.
This article is licensed under a Creative Commons Attribution-NonCommercial 3.0 Unported Licence.

Journal of Materials Chemistry A Accepted Manuscript

Introduction

The growing reliance on energy storage systems has rapidly increased, pushed by the need for decarbonisation and the efficient utilisation of green energy sources, such as solar and wind power. Among various energy storage technologies, lithium-ion systems have played a pivotal role, especially in batteries, offering the required energy storage performance owing to their high energy density and lightweight characteristics. However, concerns arise regarding specific applications, particularly in mini-grid and mini off-grid energy storage, in which cost-effectiveness, environmental safety, and sustainability is priority. Li-ion batteries possess safety issues, high costs and limited resource availability, which, alongside the use of potentially flammable electrolytes, renders them unsuitable for mini-grid and mini off-grid storage systems. One alternative which has attracted attention are aqueous zinc-ion batteries (AZIBs), emerging in response to this new demand for superior batteries. AZIBs have become a focal point of interest in the field of electrochemical energy storage due to several advantages, including the ease of manufacturing; AZIBs can be assembled in open air,[1] whereas lithium-ion batteries (and sodium ion batteries) require specialised controlled conditions, thus eliminating extra costs. Zinc itself is also more cost effective due to its high natural abundance, which is four times that of lithium, resulting in the cost of zinc ($0.5 - $1.5/lb) being significantly lower than that of lithium ($8 - $11/lb). Zinc's abundancy in the crust is 79 ppm, ranking it the fourth in the world metal production, making is a strong contender when considering resource availability (and, in turn, cost and sustainability).[2] The electrolyte used by AZIBs is more environmentally friendly, as they are mainly aqueous (if not, slightly acidic),[3] and affordable. Zinc anodes offer a high gravimetric capacity (820 mAh g^{-1}) and volumetric capacity (5855 mAh cm^{-3}),[2,4–6] along with a low redox potential (-0.762 V vs SHE). These properties make them well-suited for use in aqueous electrolytes, and the two-electron transfer process during redox reactions enables high-energy density in AZIBs.[1,2] Moreover, multivalent zinc ions can transfer two electrons which accelerates more energy storage that univalent batteries.[7] The ionic radius of zinc ions (0.74 Å) is similar to that of lithium (0.69 Å), relative to the radius of other alternatives, such as sodium, which has a radius of 1.02 Å. Thus, it can be seen clearly that AZIBs are a promising alternative to lithium-ion batteries and suitable for mini-grid and mini off-grid storage systems. Currently, there are many issues faced by AZIBs, such as zinc dendrite growth in aqueous electrolyte,[8] side reactions,[9] and cathode dissolution.[10]

View Article Online
DOI: 10.1039/D4TA06572G

Open Access Article. Published on 22 November 2024. Downloaded on 11/26/2024 9:52:47 AM.
This article is licensed under a Creative Commons Attribution-NonCommercial 3.0 Unported Licence.

Journal of Materials Chemistry A Accepted Manuscript

Cathode material in AZIBs is of high importance due to the requirement of identifying a suitable material which can facilitate the high polarisation of bivalent zinc ions,[11] thus requiring the material to possess high capacity and the appropriate structural stability to facilitate (de)intercalation of ions,[1] resulting in research into various different materials – out of which manganese and vanadium-based materials, organic compounds, and Prussian blue analogues were most promising.[11] Manganese based cathodes are considered due to their high theoretical capacity (309 mAh g^{-1}),[2] low cost and toxicity, environmentally friendliness and multivalent states,[12] however, severe capacity fading takes place due to the dissolution of manganese into electrolyte with cycling. Polyvalent manganese oxides have multiple crystal structures,[13] which provide frameworks to accommodate various cations.[12] Organic materials possess abundant chemical composition, biodegradability, affordability, multiple electron reactions and a flexible electrochemical window.[11] Currently there is limited research into organic materials for cathode use, but the results produced so far show a theoretical capacity of 335 mAh g^{-1},[14] which is similar to that of manganese based materials. Prussian blue analogues have an open framework structure[5,12] with a face centred cubic lattice, thus resulting in large ion-intercalation sites.[11] The material displays a decent cycle performance (81% retention after 100 cycles),[2] but research has shown them to yield a lower specific capacity than the other materials (55.6 mAh g^{-1}, 120 mAh g^{-1} and 100 mAh g^{-1}). [2,5,11] Though the large interstitial sites and large tunnels allow easy and reversible electrochemical insertion/extraction of Zn^{2+} ions,[15] the low theoretical specific capacity and relatively low cycle performance makes it unattractive.

On the other hand, vanadium-based materials, namely vanadium oxides, are of high interest due to the large-tunnel framework structure, presenting a potential possibility to accommodate numerous Zn^{2+} ions for storage. Vanadium pentoxide (V_2O_5) has a structure where the lattice contains covalent bonds and weak van der Waals forces and hydrogen bonds, allowing Zn^{2+} to attach and detach freely, resulting in excellent rate performance.[11] However, it suffers from instability and low capacity when subjected to repeated intercalation of ions because of the unstable single layer structure and pure +5 valence. [16,17] VO_2 in comparison has a tunnel like framework, which results in a remarkable ability for rapid Zn^{2+} (de)intercalation, displaying outstanding rate performance.[18] VO_2 has numerous polymorphs with different complex crystal frameworks,[12] but the VO_2(B) stands out on account of its distinct structure, composed by distorted VO_6 octahedra connected through edge sharing, which is able to withstand (de)intercalation of Zn^{2+} ions.[2] It is noted that overall performance of cathode materials depends not only on their inherent properties, but also on synthesis methods, electrode processing

View Article Online
DOI: 10.1039/D4TA06572G

techniques, and achieving ultra-high mass loading and hence need sequential studies to establish to standard electrode processing techniques to achieve maximum capacities during the testing and approaching to the theoretical values.

In this study, we investigate sequential synthesis methods and processing techniques for electrode materials to enhance the capacities of VO_2(B) as a cathode material. This is followed by further efforts to achieve ultra-high mass loading for attaining ultrahigh-areal capacities compared to conventional counterparts. Our research aims to demonstrate how the capacity of active materials can be improved through advanced synthesis and processing techniques of battery electrodes, thereby contributing to the development of reliable and high-performance AZIBs.

Results and Discussion

Effective mass utilisation on the cathode without losing electrode conductivity and capacity is essential for achieving high performance. **Figures 1a** and **1b** show schematics of coin cells with conventional slurry-casted cathodes on flat current collectors with an approximate thickness of 0.05 mm, while 3D ultrathick electrodes have an approximate thickness of 2.55 mm, including the carbon paper and vitreous carbon foam. Digital images of the developed ultrathick electrodes are shown in **Figure 1c**, obtained by processing optimized VO_2(B) cathode materials onto a 3D vitreous carbon foam. This 3D vitreous carbon foam framework offers advantages such as rapid Zn^{2+} ion diffusion without losing conductivity over the 3D scaffolds (**Figure 1d**), leading to superior charge storage capacities compared to conventional electrodes when normalized by area. Additionally, VO_2(B) has a tunnel-like framework (**Figure 1e**) that facilitates effective Zn^{2+} ion diffusion through tunnels in the *b*-direction and *c*-direction, resulting in extremely high capacities. **Figure 1f** shows low-magnification SEM images of the 3D cathode, while high-magnification images (**Figures 1g** and **1h**) demonstrate the decoration of VO_2(B) nanorods on the 3D current collector scaffolds.

Open Access Article. Published on 22 November 2024. Downloaded on 11/26/2024 9:52:47 AM.
This article is licensed under a Creative Commons Attribution-NonCommercial 3.0 Unported Licence.

Journal of Materials Chemistry A Accepted Manuscript

View Article Online
DOI: 10.1039/D4TA06572G

Open Access Article. Published on 22 November 2024. Downloaded on 11/26/2024 9:52:47 AM.
This article is licensed under a Creative Commons Attribution-NonCommercial 3.0 Unported Licence.

Journal of Materials Chemistry A Accepted Manuscript

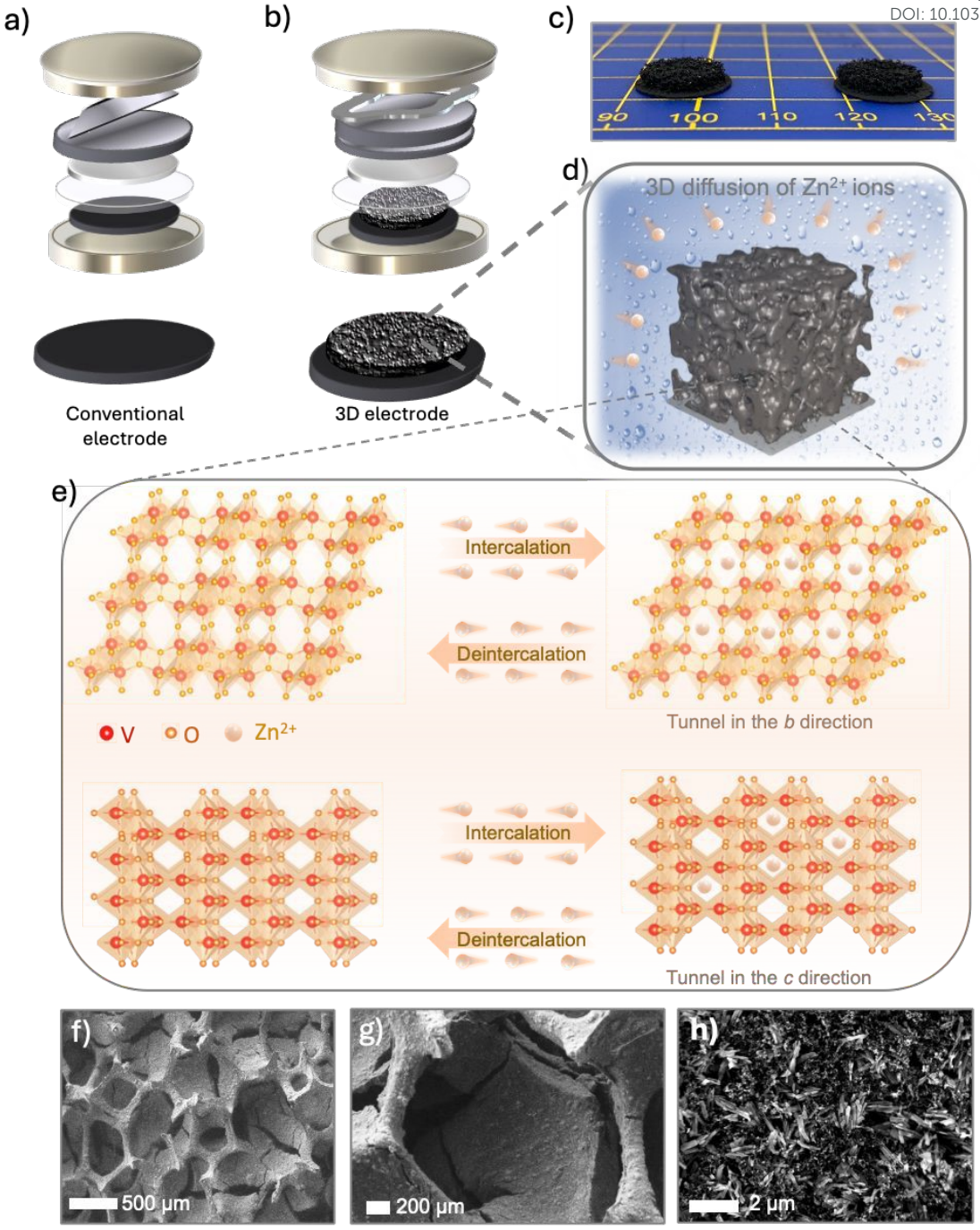

Figure 1. *Schematic of AZIB with a) a conventional, slurry casted electrode and b) a 3D, ultrathick electrode. c) A picture of the 3D electrodes assembled with the vitreous carbon foam and carbon paper, attached to d) a zoomed in schematic depiction of the 3D cathode. e) Schematic view of* Zn^{2+} *(de)intercalation* $VO_2(B)$ *nanorods projected along the b- and c-directions. f-h) SEM images of the 3D cathode at increasing magnifications.*

View Article Online
DOI: 10.1039/D4TA06572G

Open Access Article. Published on 22 November 2024. Downloaded on 11/26/2024 9:52:47 AM.
This article is licensed under a Creative Commons Attribution-NonCommercial 3.0 Unported Licence.

Journal of Materials Chemistry A Accepted Manuscript

Synthesis Methods

It is noted that the capacity of VO_2(B) material depends not only on the electrode processing but also on the synthesis process. To obtain optimum capacities of VO_2(B), we explored both conventional hydrothermal synthesis and a rapid multiwave reaction process. The specific synthesis conditions are detailed in the experimental section (Supplementary Information). **Figure 2a** shows the SEM image of VO_2(B) obtained using the multiwave reaction process, where multiwave digestion produced nanorods alongside clusters. The TEM image in **Figure 2b** further supports this observation. The HRTEM image in **Figure 2c** demonstrates the calculated d-spacing value of 0.265 nm corresponding to the (-3 1 1) planes in the monoclinic structure of VO_2(B). In contrast, the hydrothermal synthesis produced uniform nanorod morphologies, as shown in **Figures 2d** and **2e**, with calculated d-spacing values of 0.351 nm corresponding to the (1 1 0) planes (Figure 2f) in the monoclinic structure of VO_2(B). These d-spacings match that of the XRD spectra, and both planes produce strong peaks in the spectra. The XRD spectra (**Figure 2g**) obtained display identical patterns for both methods, with the corresponding planes indicated. From the MDI Jade XRD data base, the correct peaks for VO_2(B) are displayed, including the strong peaks at $2\theta = 14.4^o$, 15.4^o, 25.2^o, 29.0^o, 30.1^o, 44.1^o, 44.9^o and 49.2^o, which corresponds to the (001), (200), (110), (002), (-401), (003), (-601) and (020) miller indices.[19] The correct phase was obtained, especially via hydrothermal synthesis, as every peak with an intensity above 5 is displayed, and the two peaks at 14^o and 15^o (approx.) are visible, which is not exhibited in the other phases of VO_2(B).[20] Additionally, V_2O_5 has not been produced, as though the XRD spectra are similar, VO_2(B) exhibits the highest intensity in the (110) peak, whereas V_2O_5 shows the highest intensity in the (001) peak.[21] The hydrothermally synthesised VO_2(B) exhibits sharper peaks than the multiwave reacted VO_2(B), indicating a higher degree of crystallinity.[22,23]

To further ensure the VO_2(B) material was as expected, Raman spectra of the materials were obtained **(Figure 2h)**, from which all the expected Raman peaks were visible in the spectrum for both samples.[24,25] The peaks at 139 cm^{-1} and 191 cm^{-1} represent the layered lattice structure. The 282 cm^{-1} and 404/406 cm^{-1} peaks represent the V=O bending vibration bonds, while the peak at 668 cm^{-1} represents the V-O-V stretching mode, resulting from the corner-shared oxygens of two pyramids. The peak at 990.60 cm^{-1} represents the terminal oxygen (V=O) stretching vibration.[24] The presence of water molecules was investigated by TGA analysis, under nitrogen flow, of the two differently synthesised VO_2(B), depicted in **Figure 2i**, in which

View Article Online
DOI:10.1039/D4TA06572G

both samples exhibit a mass loss up to approx. 375 °C (0.9 wt% for multiwave VO_2(B) and 1 wt% for hydrothermal VO_2(B)). The weak weight loss (< 1%) implied there was no lattice water that could have been present originally during the stabilisation of the VO_2(B) intermediate structure. Additionally, as the weight was very nearly constant, it indicated that in the N_2 atmosphere, VO_2(B) can be stable.[26,27]

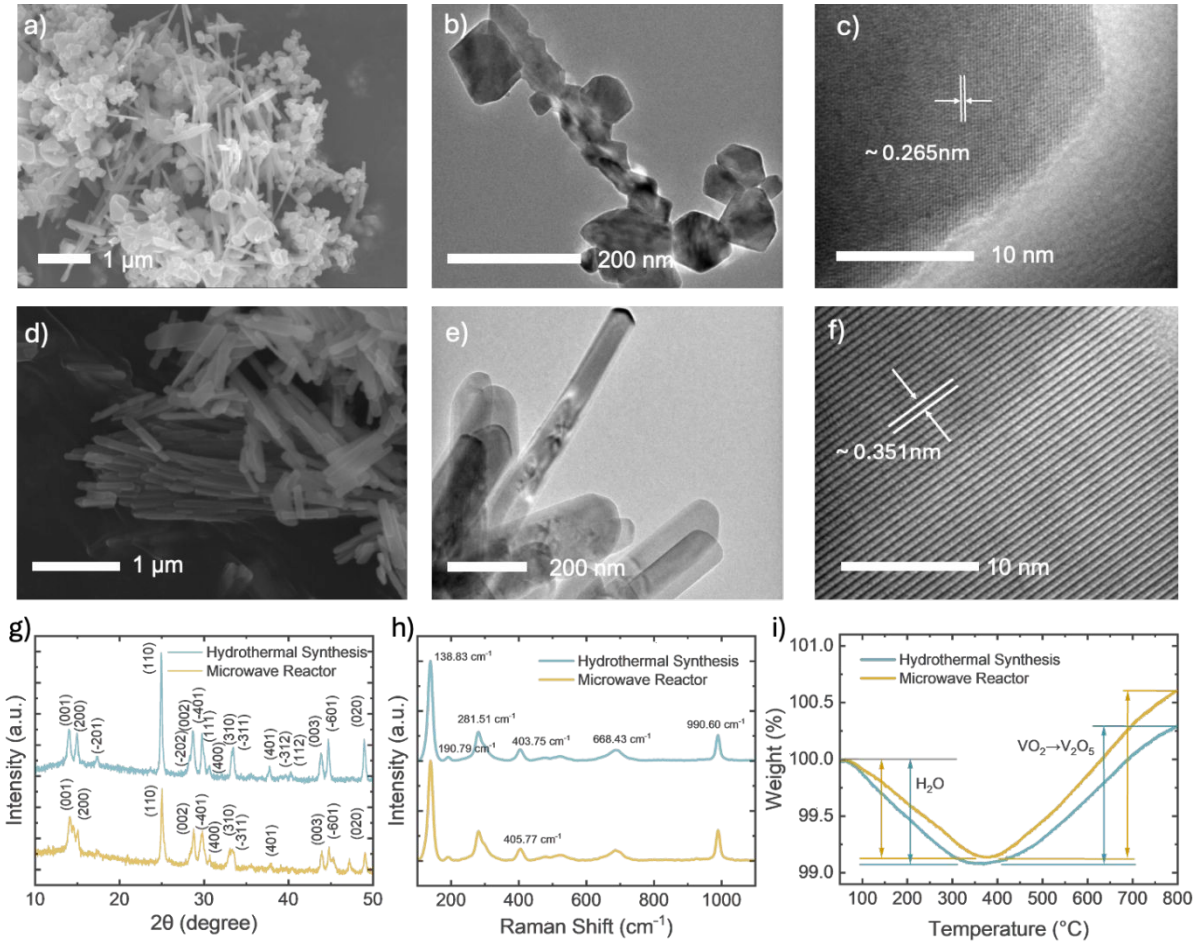

Figure 2. *SEM, TEM and HRTEM images of (a-c) multiwave digested and (d-f) hydrothermal synthesised VO_2(B). TEM and HRTEM images of (b, c) multiwave digested and (e, f) hydrothermal synthesised VO_2(B). (g) XRD, (h) Raman spectra and (i) TGA profiles of the two VO_2(B) samples*

XPS analysis was conducted to further confirm the transformation of oxidation number of vanadium, alongside identifying which sample had more oxygen vacancies. **Figure 3** displays the XPS Spectra of the two samples: in **Figures 3a** and **c**, the binding energy is at E_B ($V_{3/2p}$) = 517.8 eV and 517.9 eV, respectively, as this is where the peak is positioned, which corresponds to the V^{5+} cations. The V^{4+} cations correspond to the binding energies of 516.7 and 524.3 eV.[28,29] The ratio between the peak area of V^{4+}/V^{5+} for the multiwave digested sample is 6.56,

Open Access Article. Published on 22 November 2024. Downloaded on 11/26/2024 9:52:47 AM.
This article is licensed under a Creative Commons Attribution-NonCommercial 3.0 Unported Licence.

Journal of Materials Chemistry A Accepted Manuscript

View Article Online
DOI: 10.1039/D4TA06572G

and for the hydrothermally synthesised sample it is 7.33, confirming a higher concentration of V^{4+} in the hydrothermally synthesised VO_2(B) (which implied more of the reactants have changed from V_2O_5 to VO_2), but it is a very small discrepancy. In **Figures 3b** and **d**, the oxygen component can be observed; the peaks at 530.5 eV and 530.4 eV correspond to the lattice oxygen, and the smaller peaks at 531.6 eV and 531.7 eV (respectively) represent the oxygen absorbed.[30,31] The area of the V-OH peak for the multiwave VO_2(B) is 13767.6, which is larger than that of the hydrothermal VO_2(B) (12982.2), thus suggesting that the hydrothermally synthesised VO_2(B) has a lower oxygen concentration (more oxygen vacancies), resulting in more efficient for (de)intercalation of Zn^{2+} ions. BET analysis was undertaken to investigate which synthesis method produced VO_2(B) with a larger surface area. **Figure S1** displays the N_2 adsorption and desorption isotherms of VO_2(B) synthesised hydrothermally and multiwave reacted. The curves suggest that both samples exhibit type III isotherms, which was expected as both are VO_2(B), implying that the c value (BET constant) is less than 1 due to the type of isotherm. The BET constant relates to the adsorption energy of the first monolayer – as it is less than 1, it shows the formation of a multilayer with no monolayer as there is no asymptote in the curve. [32,33] Additionally, surface area tests were performed on the samples, which show that the measured specific surface areas were 23.88 $m^2\ g^{-1}$ for the multiwave sample and 24.49 $m^2\ g^{-1}$ for the hydrothermal sample, confirming that there's no significant difference in the surface areas between the two, which was further supported by the lack of significant difference between the absorbed volume (the hydrothermally synthesised VO_2(B) absorbed a slightly larger volume of approx. 5$cm^3\ g^{-1}$ more).

Open Access Article. Published on 22 November 2024. Downloaded on 11/26/2024 9:52:47 AM.
This article is licensed under a Creative Commons Attribution-NonCommercial 3.0 Unported Licence.

Journal of Materials Chemistry A Accepted Manuscript

View Article Online
DOI: 10.1039/D4TA06572G

Open Access Article. Published on 22 November 2024. Downloaded on 11/26/2024 9:52:47 AM.
This article is licensed under a Creative Commons Attribution-NonCommercial 3.0 Unported Licence.

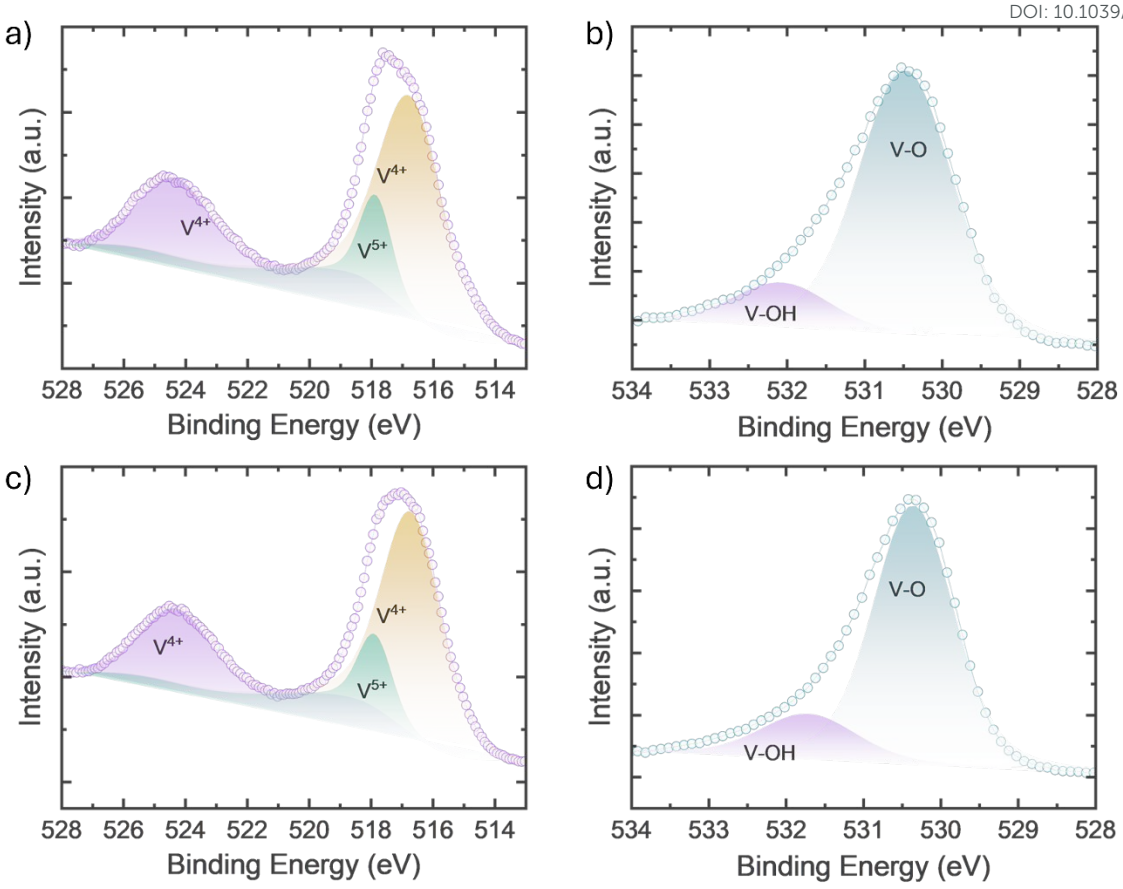

Figure. 3. *XPS Spectra of (a, b) multiwave digested and (c, d) hydrothermally synthesised VO_2(B) – (a, c) V2p and (b, d) O1s.*

Next, the electrochemical performance of the two samples was evaluated in coin cells using a conventional electrode configuration, as described in the experimental section (Supporting Information). Comparative cyclic voltammetry (CV) and galvanostatic charge-discharge (GCD) measurements were taken of cells assembled with hydrothermal and multiwave synthesised VO_2(B) cathodes. Initially, a conventional mass loading was employed and was kept relatively the same to allow for uniformity in comparison between the samples. CVs were measured at different scan rates (0.2 – 1.0 mV s^{-1}) and in a specific voltage window (0.2 – 1.6V). In **Figures 4a** and **b**, the CVs display two cathodic and two anodic peaks, corresponding to the intercalation and deintercalation reactions occurring. Two anodic peaks can be seen at approximately 0.7 V and 1.1 V, and the cathodic peaks positioned at approx. 0.5 V and 0.9 V. The two peaks indicate two different Zn^+ insertion/extraction processes, thus confirming the redox reaction of VO_2(B) during discharge/charge.[34] Equation 1 and 2 describe the electrochemical reaction of the Zn/VO_2 battery, with Eqn. 1 being the cathode and Eqn. 2 the anode.[35]

Journal of Materials Chemistry A Accepted Manuscript

View Article Online
DOI: 10.1039/D4TA06572G

$$VO_2(B) + xZn^{2+} + 2xe^- \leftrightarrow Zn_xVO_2(B) \quad (1)$$

$$Zn \leftrightarrow Zn^{2+} + 2e^- \quad (2)$$

Alongside the H^+ ion intercalation, (de)doping processes may take place. When the cathode is discharged, H^+ ions from the electrolyte diffuse into the VO_2(B) structure, which is known as H^+ insertion. Dedoping is the release of H^+ back into the electrolyte when charged.[36] The CV curves obtained indicated that cathodes made with hydrothermally synthesised VO_2 exhibit sharper peaks, with two clear peaks for each Zn^+ process, and an overall slightly higher specific capacity. Due to the sharp peaks, the potential difference (peak separation) is smaller, implying a highly reversible redox rection and efficient charge storage processes. Ex-situ charge/discharge tests on the cells were run to different voltages, as seen in **Figure S2a**, which was followed by Raman measurements. When the AZIB discharges, Zn^{2+} from the anode are stripped and then intercalated into cathode. Therefore, the cathode material (VO_2(B)) is being reduced, changing from V^{4+} to V^{3+}. It's likely that VO_2(B) has undergone a phase transition when discharged, from a monoclinic to tetragonal structure. This phase transition involves significant rearrangement of atoms and bond length and angles. When the cell is discharged to 0.2V, a peak appears at approx. 800-1000 cm^{-1}, which could be due to the carboxylic acid dimer forming, alongside C-C aliphatic chains and C-O-C bonds forming.[37,38] Another, broad peak appears at approx. 500 cm^{-1}, which is seen in the VO_2(A) phase, due to its tetragonal structure which is not visible in the VO_2(B) spectra, which further supports the theory that VO_2(B) undergoes a phase transition when discharged fully.[37,39] When the cell is charged, the cathode is oxidised, returning the vanadium to its usual oxidation state of +4, due to the Zn^{2+} ions deintercalating and returning to the electrolyte.[40]

Open Access Article. Published on 22 November 2024. Downloaded on 11/26/2024 9:52:47 AM.
This article is licensed under a Creative Commons Attribution-NonCommercial 3.0 Unported Licence.

Journal of Materials Chemistry A Accepted Manuscript

View Article Online
DOI: 10.1039/D4TA06572G

Open Access Article. Published on 22 November 2024. Downloaded on 11/26/2024 9:52:47 AM.
This article is licensed under a Creative Commons Attribution-NonCommercial 3.0 Unported Licence.

Journal of Materials Chemistry A Accepted Manuscript

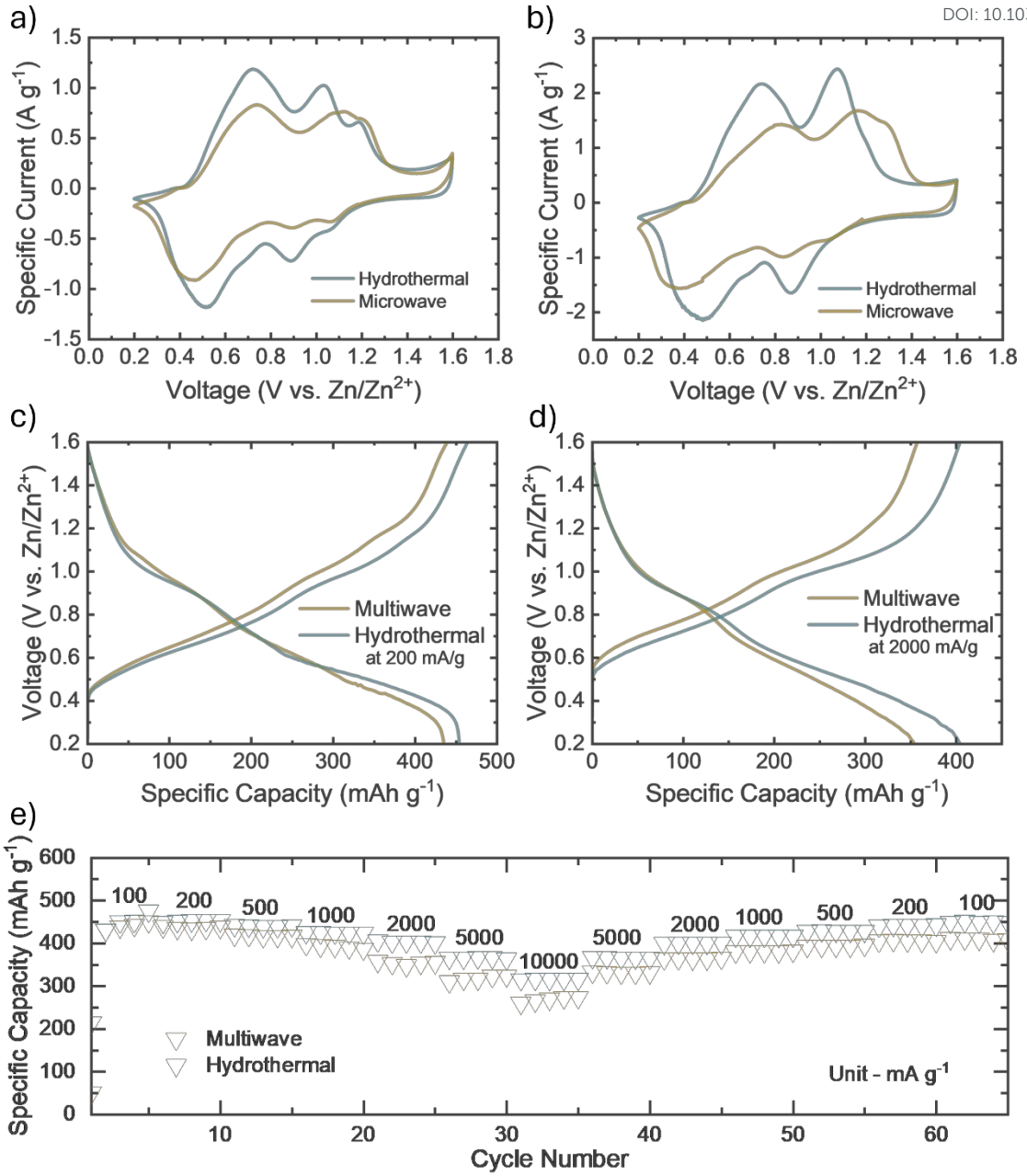

Figure. 4. *Comparative CV curves of AZIBs at scan rates of (a) 0.5 mV s^{-1} and (b) 1.0 mV s^{-1}. GDCs curves at specific currents (c) 200 mA g^{-1} and (d) 2000 mA g^{-1}. (e) Rate capacity tests for AZIBs, with cathodes synthesised via hydrothermal and multiwave synthesis.*

GCD measurements were taken at different specific currents, ranging from 100 to 10,000 mA g^{-1}, to evaluate the electrochemical performance of the materials. It's observed that the specific capacities of hydrothermally synthesised VO_2(B) are greater than those of the multiwave digested samples, which is in agreement with the CV results. For example, the multiwave-treated sample exhibits specific capacities of 435 mAh g^{-1} and 353 mAh g^{-1} at specific currents of 200 mA g^{-1} and 20,000 mA g^{-1}, respectively. These capacities increase to 454 mAh g^{-1} and

View Article Online
DOI: 10.1039/D4TA06572G

404 mAh g^{-1} for the hydrothermally synthesised VO_2(B), as shown in **Figures 4c** and **4d** consistent with the trends indicated by the CV graphs. Moreover, **Figure 4e** illustrates a comparison of rate capacity tests, showing that the cell with the hydrothermal VO_2(B) cathode achieved higher specific capacities across all tested specific currents, whether low or high. This suggests that the overall electrochemical performance is better, likely due to the increase in number of oxygen vacancies and higher concentration of V^{4+} in the hydrothermal samples, which could enable more efficient intercalation of Zn^{2+} ions compared to the multiwave reactor samples. Additionally, we conducted long-term cycling tests on the coin cells to assess their stability, applying a specific current of 1000 and 2000 mA g^{-1}. Both cells performed reliably for 500 cycles, but the hydrothermally synthesised VO_2(B) cathode exhibited a higher specific capacity (346 mAh g^{-1}) compared to the multiwave reacted VO_2(B) cathode (261 mAh g^{-1}), as shown in **Figure S3.** Both cells exhibited a slight decrease in specific capacity over time, with the hydrothermal cell undergoing an activation period, likely due to further material activation during cycling. However, based on the data and methods presented, the hydrothermally synthesised VO_2(B) was determined to be the optimal material. Consequently, the hydrothermal method was exclusively employed from this point onward.

Drying Methods

The identified optimal hydrothermal synthesis method was further developed, achieving relatively higher mass loading (~ 4.0 mg/cm^2). Additionally, the study aimed to understand how different electrode drying processes (freeze drying and conventional oven drying) influence charge storage performance. The CV curves at different scan rates of the oven and freeze-dried cells can be seen in **Figures 5a** and **b**. In **Figures 5c** and **d**, for high mass loading (~ 4.0 mg/cm^2), the freeze-dried cathode outperforms the oven dried one significantly, which implied the porosity of the material was increased via the freeze drying (see further). The freeze-dried cathode yields a specific current at each peak that is larger than that of the oven dried, as they are also greater in magnitude. **Figure S4** displays the CV curves for that of low mass loading cathodes (~1.5 mg/cm^2), and still the freeze-dried cathode performed the best, with the discrepancy between the specific currents obtained increasing as the scan rates increased. For each mass loading, the freeze-dried cathodes performed the best, yielding a higher specific current and sharper peaks, indicating the two intercalation processes. This supports the theory that the freeze-dried electrode has increased porosity, thus increases surface area, resulting in more movement of ions (see further).

Open Access Article. Published on 22 November 2024. Downloaded on 11/26/2024 9:52:47 AM.
This article is licensed under a Creative Commons Attribution-NonCommercial 3.0 Unported Licence.

Journal of Materials Chemistry A Accepted Manuscript

View Article Online
DOI: 10.1039/D4TA06572G

Assuming the peak current (i) obeys a power law relationship with the scan rate (v), in principle, they will have the relation;

$$i(V) = av^b \quad (3)$$

$$\Longrightarrow \log(i) = \log(a) + b \times \log(v) \quad (4)$$

Where a and b are variable parameters.[41,42]

Equation 4 can be viewed as the equation for a linear relationship. If the b value ≈ 0.5, the electrochemical process is diffusion controlled, whereas if the b value ≈ 1.0, it indicates a capacitive controlled dominant process.[41] **Figure S5** displays the calculated b values for the peaks, which decreased as the mass loading of the cathode increased, implying the electrochemical process is moving from a capacitive controlled process to a diffusion controlled one, which is expected because as the mass loading increases, so does the thickness of the cathode, thus requiring more diffusion of the ions. The b values in **Table S1** also indicate that the freeze-dried cathode is more capacitive controlled than the oven dried one, when comparing similar mass loading, which could be due to the increased porosity of the freeze-dried cathode and effective intercalation of ions. Lastly, the b values for the right-hand anodic peak (b) are always larger than that of the first (a), similarly, the right-hand cathodic peak (c) has larger b values than the left cathodic peak (d), meaning the first intercalation step is more diffusive, as is the last deintercalation step. This is because initially the ions need to overcome a higher diffusion barrier due to the initial structure of the electrode, nucleation and concentration limitations. The last deintercalation peak (d) also exhibits this as the Zn^{2+} ions are in low concentration, the diffusion path is increased as the remining ions are embedded deeper with in the cathode structure, structural changes undergo, and polarisation further slows ion transport.[43,44] Moreover, the cross-sectional SEM images (**Figures 5e** and **5f)** of the cathodes display that the freeze drying has increased porosity of the cathode material. Furthermore, high magnification SEM images were obtained (as seen in **Figure S6**), in which it can be seen that freeze drying has produced a more porous material, whereas the oven dried sample has numerous relatively large clusters of VO_2(B), which reduces surface area. The pores observed are relatively uniformly formed and there are many – this could justify why the freeze-dried cathode cells perform better (larger surface area for ion movement).

Open Access Article. Published on 22 November 2024. Downloaded on 11/26/2024 9:52:47 AM.
This article is licensed under a Creative Commons Attribution-NonCommercial 3.0 Unported Licence.

Journal of Materials Chemistry A Accepted Manuscript

View Article Online
DOI: 10.1039/D4TA06572G

Open Access Article. Published on 22 November 2024. Downloaded on 11/26/2024 9:52:47 AM.
This article is licensed under a Creative Commons Attribution-NonCommercial 3.0 Unported Licence.

Journal of Materials Chemistry A Accepted Manuscript

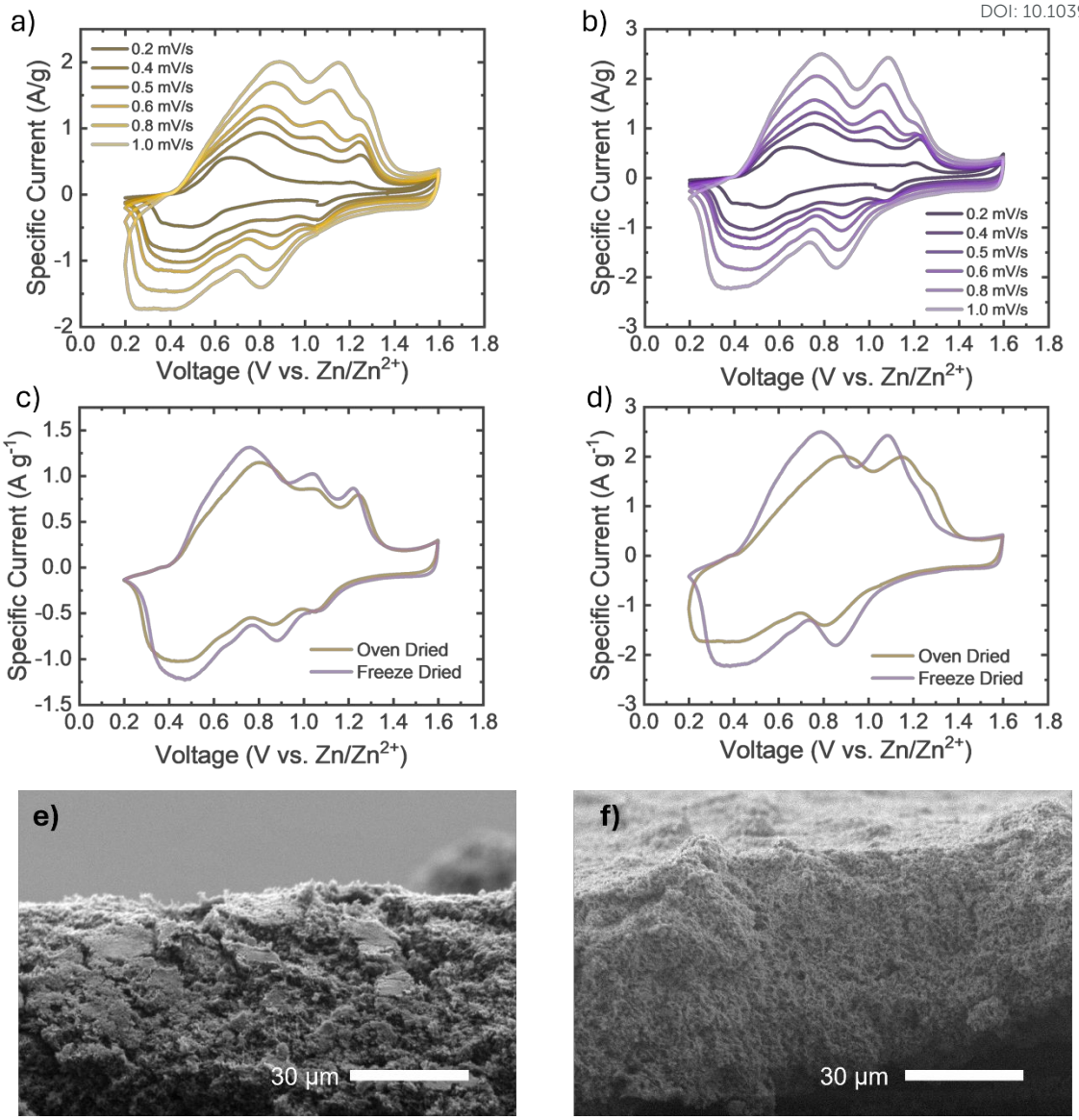

Figure. 5 *Full CV curves of high mass cathodes dried by a) vacuum oven and b) freeze dryer. Comparative CV curves of drying methods at a scan rate of c) 0.5 mV s^{-1} and d) 1.0 mV s^{-1}. SEM images of VO_2(B) cathodes synthesised by e) oven and f) freeze drying.*

Electrochemical impedance spectroscopy measurements were taken to determine the internal resistance of the cell, assembled with differently dried cathodes. **Figure 6a** displays the Nyquist plots of AZIBs with oven and freeze-dried cathodes with a high mass loading. The cells have a relatively similar equivalent series resistance (ESR) as the first values on the x axis are very similar, meaning there is similar total resistance, resulting in similar response times. [18,40,41]As the charge transfer resistance is lower in the oven dried sample compared to the vacuum dried one, it suggests that the redox reaction occurring at the cathode is quicker in vacuum dried compared to that of oven dried electrodes.[45]

View Article Online
DOI: 10.1039/D4TA06572G

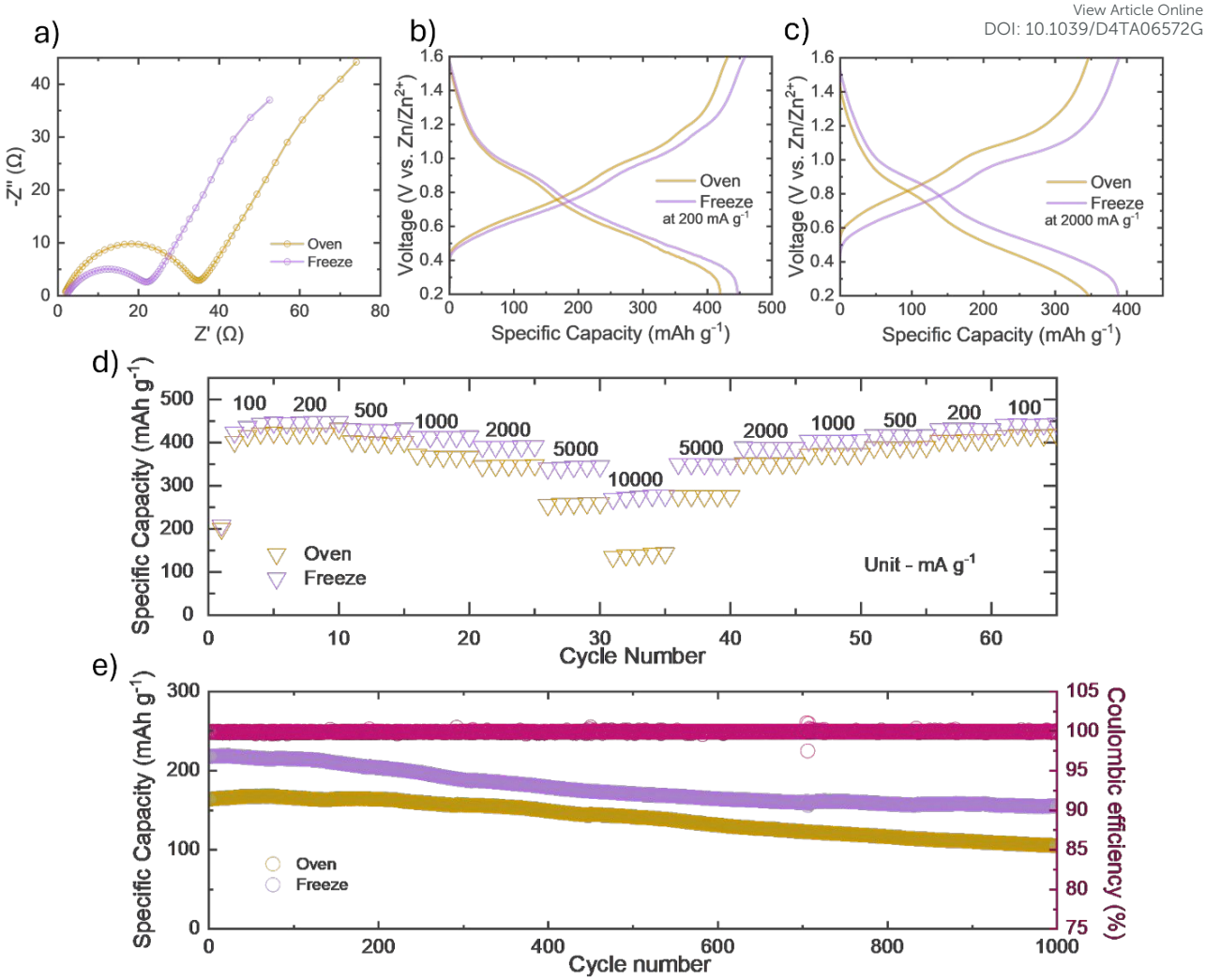

Figure. 6. *a) Nyquist plot of AZIBs with oven and freeze-dried cathodes with high mass loading. Comparative GCD curves of high mass loading cathodes, comparing drying methods at a specific current of b) 200 mA* g^{-1} *and c) 200 mA* g^{-1}*. d) Rate tests comparison of high mass, oven and freeze dried* VO_2*(B) cathodes. Long-term cycling of AZIBs with cathodes dried by different methods at e) 2000 mA* g^{-1}*.*

Moreover, GCD curves were obtained, alongside rate capacity plots, to analyse the specific capacity of the cells. **Figures 6b**, **c** and **d** display that for both drying methods of the cathode with a high mass loading. High capacities of 447 mAh g^{-1}, and 421 mAh g^{-1} were obtained for the freeze and oven dried cells, respectively, at 200 mA g^{-1}, which dropped to 388 mAh g^{-1} and 347 mAh g^{-1} at 2000 mA g^{-1}, respectively. It can be observed that at relatively lower specific currents, the difference in capacities between freeze-dried and oven-dried electrodes is minimal. However, at higher specific currents (e.g., 10000 mA g^{-1}), freeze-dried electrodes exhibit significantly higher specific capacitance (276.8mAh g^{-1}) compared to oven-dried electrodes (143.5mAh g^{-1}). This implied that the drying method directly affects cell

Open Access Article. Published on 22 November 2024. Downloaded on 11/26/2024 9:52:47 AM.
This article is licensed under a Creative Commons Attribution-NonCommercial 3.0 Unported Licence.

Journal of Materials Chemistry A Accepted Manuscript

View Article Online
DOI: 10.1039/D4TA06572G

Open Access Article. Published on 22 November 2024. Downloaded on 11/26/2024 9:52:47 AM.
This article is licensed under a Creative Commons Attribution-NonCommercial 3.0 Unported Licence.

Journal of Materials Chemistry A Accepted Manuscript

performance, as expected. Thus, the freeze-drying process is more effective for achieving rate capability in batteries while also offering higher capacity at relatively higher mass loading (**Figure 6d**). Furthermore, **Figure 6e** illustrates the long-term cycling performance of the electrodes. It shows that freeze-dried electrodes maintained higher specific capacities compared to oven-dried electrodes. After 1000 cycles, the specific capacities measured are 155.8mAh g^{-1} for freeze-dried electrodes and 105.7mAh g^{-1} for oven-dried electrodes, with capacity retentions of 71.3% and 64.4% respectively. Better capacities were observed in the freeze dried electrode cells than the oven dried cell when the applied specific current is increased, which could be due to the increased surface area of the freeze dried cathode allowing more (de)intercalation of ions in the same, short period of time (when comparing to 1000 mA g^{-1}), thus supporting the porosity theory of the freeze dried cathode overcoming the limited depth penetration issue of ultrathick cathodes.

Ultrathick electrodes

The comparison of drying methods consolidated the theory that porosity of the cathode directly relates to the improvement of the cell's performance when concerning high mass loading, as the freeze-dried cathodes have increased porosity, as discussed. This theory was now applied to ultrathick (2.55 mm, as seen in **Figure S7**) with ultra-high mass loading (~ 24 mg/cm^2) cathodes, which were based on carbon paper and a porous vitreous carbon foam (the porosity expected to increase surface area, similarly to the working principle of the freeze-drying method). First, we performed cyclic voltammetry (CV) on the ultra-thick cathodes, as shown in **Figures S8a** and **b**, which demonstrated distinct redox peaks as expected. **Figure S8c** displays the GCD curves of the ultra-thick cathodes at different areal currents. Notably, the ultra-thick 3D cathode exhibits impressive charge storage performance, with significantly higher areal capacities compared to the conventional cathode. The measured areal capacitances are 4.15 mAh/cm^2 and 0.63 mAh/cm^2 at areal currents of 1 mA/cm^2 and 10 mA/cm^2, respectively, which drop to 0.91 mAh/cm^2 and 0.21 mAh/cm^2 for conventional cathodes (**Figures 7a** and **7b**). The rate tests (**Figure 7c**) further confirmed the impressive charge storage performance of our ultra-thick 3D cathodes compared to the conventional cathode. Moreover, long-term cycling tests revealed that the cell with the 3D cathode remained stable for 1000 cycles, retaining 81.7% capacity (**Figure 7d)**, consolidating the structural and electrochemical stability of the 3D cathodes as expected. The porous vitreous carbon foam structure clearly enhanced the mechanical stability of the cell, which was further improved by enclosing the

View Article Online
DOI: 10.1039/D4TA06572G

cathode two acrylic rings, each with a thickness of 0.8 mm, to maintain its mechanical structure, as seen in **Figures S7a** and **b**.

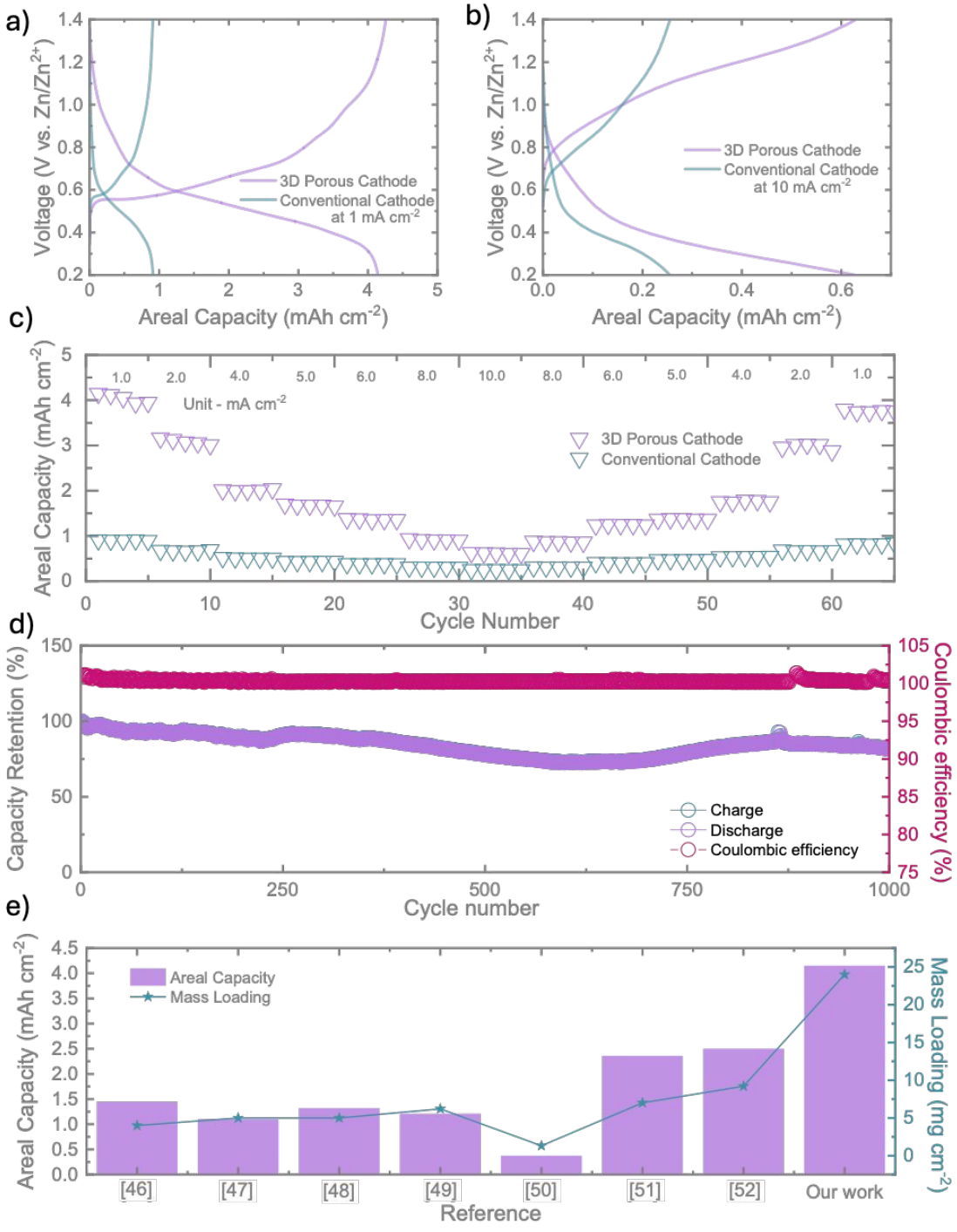

Figure. 7. *Comparative GCD curves of 3D and conventional cathode cells with an applied areal currents of a) 1 mA/cm² and b) 10 mA/cm². c) Rate tests comparison of cathodes at different applied areal currents. d) Long-term cycling capacity retention of AZIB with 3D*

Open Access Article. Published on 22 November 2024. Downloaded on 11/26/2024 9:52:47 AM.
This article is licensed under a Creative Commons Attribution-NonCommercial 3.0 Unported Licence.

Journal of Materials Chemistry A Accepted Manuscript

View Article Online
DOI: 10.1039/D4TA06572G

cathode. e) Comparison of areal capacities at an applied current of 1 mA cm² of this work with current results reported.[46–52]

Finally, we compared the performance of our ultra-thick cathodes with those reported in the literature (as shown in **Figure 7e**).[46–52] The most similar works still lack in comparison to our work; Zhang, H. *et al*[49] fabricated a cathode made of oxygen deficient $ZnMn_2O_4$, with a mass loading of 6.2 mg cm^{-2}, yielding an areal capacity of 1.21 mAh cm^{-2}; Fang, K. *et al*[51] developed a high mass loading, binder free, flexible vanadium oxide cathode, with a mass loading of ~7 mg cm^{-2} and an areal capacity of 2.36 mg cm^{-2}. Lastly, Yang, H. *et al*[52] 3D printed carbon microlattices, over which MnO_2 was deposited over to create the cathode for the ZIB, with a mass loading of 9.2 mg cm-^{2}, obtaining an areal capacity of 2.5 mA cm^{-2} (all capacities were obtained at an applied current of 1 mA cm^{-2}). In our work, the mass loading was increased significantly, and the effect can be seen; no other work has obtained an areal capacity similar to that which we have produced, consolidating the theory that increased mass loading of active material increases the surface area and, in turn, the number of sites for charge storage processes, thus increasing the capacity yielded. This comparison clearly demonstrates that our approach yields higher charge storage performance than the reported values. This further confirms that our synthesis and processing methods for materials and electrodes play a significant role in enhancing overall charge storage performance.

Conclusion

This study conducts a step-by-step investigation of material synthesis methods, electrode processing, and the fabrication of 3D cathodes. Our findings suggest that hydrothermal synthesis of VO_2(B) cathodes results in superior charge storage performance. This enhancement is attributed to the morphology formed, increased oxygen vacancies, and a greater concentration of V4+ in the hydrothermal samples, which may facilitate more efficient Zn^{2+} ion intercalation compared to samples from the multiwave reactor. Electrochemical tests further confirm that freeze-dried cathodes demonstrate improved performance, owing to their larger surface area that promotes enhanced ion (de)intercalation and mobility, leading to faster charge transfer rates. The mass loading of the active material is a critical factor in cell performance; initially, as mass loading increases, cell performance improves. However, beyond a certain point, excessive mass loading leads to performance degradation, likely due to crack formation during the cathode drying process, limited ion penetration depth, and reduced overall conductivity of the electrodes. Introducing a 3D porous cathode offers a promising

Open Access Article. Published on 22 November 2024. Downloaded on 11/26/2024 9:52:47 AM.
This article is licensed under a Creative Commons Attribution-NonCommercial 3.0 Unported Licence.

Journal of Materials Chemistry A Accepted Manuscript

View Article Online
DOI: 10.1039/D4TA06572G

solution, as its large surface area prevents excessive slurry buildup, improves ion penetration, and results in higher areal capacities.

Open Access Article. Published on 22 November 2024. Downloaded on 11/26/2024 9:52:47 AM.
This article is licensed under a Creative Commons Attribution-NonCommercial 3.0 Unported Licence.

Journal of Materials Chemistry A Accepted Manuscript

View Article Online
DOI: 10.1039/D4TA06572G

References

1 W. Du, E. H. Ang, Y. Yang, Y. Zhang, M. Ye and C. C. Li, *Energy Environ Sci*, 2020, **13**, 3330–3360.

2 L. Chen, Q. An and L. Mai, *Adv Mater Interfaces*, DOI:10.1002/ADMI.201900387.

3 J. Ming, J. Guo, C. Xia, W. Wang and H. N. Alshareef, *Materials Science and Engineering: R: Reports*, 2019, **135**, 58–84.

4 G. Fang, J. Zhou, A. Pan and S. Liang, *ACS Energy Lett*, 2018, **3**, 2480–2501.

5 C. Li, X. Zhang, W. He, G. Xu and R. Sun, *J Power Sources*, 2020, **449**, 227596.

6 M. Zhang, R. Liang, T. Or, Y.-P. Deng, A. Yu and Z. Chen, *Small Struct*, 2021, **2**, 2000064.

7 R. K. Guduru and J. C. Icaza, *Nanomaterials 2016, Vol. 6, Page 41*, 2016, **6**, 41.

8 W. Bi, J. Chai, L. Meng, Z. Li, T. Xiong, J. Shu, X. Yao and Z. Peng, *ACS Appl Mater Interfaces*, 2023, **15**, 25594–25603.

9 J. R. Loh, J. Xue and W. S. V. Lee, *Small Methods*, 2023, **7**, 2300101.

10 T. Mageto, S. D. Bhoyate, K. Mensah-Darkwa, A. Kumar and R. K. Gupta, *J Energy Storage*, 2023, **70**, 108081.

11 B. Tang, L. Shan, S. Liang and J. Zhou, *Energy Environ Sci*, 2019, **12**, 3288–3304.

12 T. Zhou, L. Zhu, L. Xie, Q. Han, X. Yang, L. Chen, G. Wang and X. Cao, *J Colloid Interface Sci*, 2022, **605**, 828–850.

13 T. R. Juran, J. Young and M. Smeu, *Journal of Physical Chemistry C*, 2018, **122**, 8788–8795.

14 Q. Zhao, W. Huang, Z. Luo, L. Liu, Y. Lu, Y. Li, L. Li, J. Hu, H. Ma and J. Chen, *Sci Adv*, DOI:10.1126/SCIADV.AAO1761.

15 M. Song, H. Tan, D. Chao, H. Jin Fan, M. Song, H. Tan, D. Chao and H. J. Fan, *Adv Funct Mater*, 2018, **28**, 1802564.

16 T. Wei, Q. Li, G. Yang and C. Wang, *J Mater Chem A Mater*, 2018, **6**, 8006–8012.

17 B. Tang, J. Zhou, G. Fang, S. Guo, X. Guo, L. Shan, Y. Tang and S. Liang, *J Electrochem Soc*, 2019, **166**, A480–A486.

18 J. Ding, Z. Du, L. Gu, B. Li, L. Wang, S. Wang, Y. Gong and S. Yang, *Advanced Materials*, 2018, **30**, 1800762.

19 MDI Materials Data, 2019, preprint, Pro.

20 B. R. An, G. D. Lee, D. H. Son, S. H. Lee and S. S. Park, *Applied Chemistry for Engineering*, 2013, **24**, 611–615.

21 C. Londoño Calderón, C. Vargas hernandez and J. Jurado, *Revista Mexicana de Fisica*, 2010, **56**, 411–415.

22 B. Deka Boruah, A. Mathieson, S. K. Park, X. Zhang, B. Wen, L. Tan, A. Boies and M. De Volder, *Adv Energy Mater*, 2021, **11**, 2100115.

Open Access Article. Published on 22 November 2024. Downloaded on 11/26/2024 9:52:47 AM.
This article is licensed under a Creative Commons Attribution-NonCommercial 3.0 Unported Licence.

Journal of Materials Chemistry A Accepted Manuscript

View Article Online
DOI: 10.1039/D4TA06572G

23 S. Milošević, I. Stojković, S. Kurko, J. G. Novaković and N. Cvjetićanin, *Ceram Int*, 2012, **38**, 2313–2317.

24 H. F. Xu, Y. Liu, N. Wei and S. W. Jin, *Optik (Stuttg)*, 2014, **125**, 6078–6081.

25 J. Chen, B. Xiao, C. Hu, H. Chen, J. Huang, D. Yan and S. Peng, *ACS Appl Mater Interfaces*, 2022, **14**, 28760–28768.

26 J. C. Valmalette and J. R. Gavarri, *Materials Science and Engineering: B*, 1998, **54**, 168–173.

27 H. Ji, D. Liu, H. Cheng, C. Zhang, L. Yang and D. Ren, *RSC Adv*, 2017, **7**, 5189–5194.

28 N. Wang, Y. Zhang, T. Hu, Y. Zhao and C. Meng, *Current Applied Physics*, 2015, **15**, 493–498.

29 M. C. Biesinger, L. W. M. Lau, A. R. Gerson and R. S. C. Smart, *Appl Surf Sci*, 2010, **257**, 887–898.

30 Y. Fu, Y. Liu, K. Ma, Z. Ji, W. Mai and C. Zhao, *J Alloys Compd*, 2020, **819**, 153063.

31 M. J. Powell, I. J. Godfrey, R. Quesada-Cabrera, D. Malarde, D. Teixeira, H. Emerich, R. G. Palgrave, C. J. Carmalt, I. P. Parkin and G. Sankar, *Journal of Physical Chemistry C*, 2017, **121**, 20345–20352.

32 A. R. B. P.M. V. Raja, BET surface area analysis of nanoparticles, https://chem.libretexts.org/Bookshelves/Analytical_Chemistry/Physical_Methods_in_Chemistry_and_Nano_Science_(Barron)/02%3A_Physical_and_Thermal_Analysis/2.03%3A_BET_Surface_Area_Analysis_of_Nanoparticles, (accessed 11 May 2024).

33 N. Wang, Y. Zhang, T. Hu, Y. Zhao and C. Meng, *Current Applied Physics*, 2015, **15**, 493–498.

34 Z. Li, S. Ganapathy, Y. Xu, Z. Zhou, M. Sarilar, M. Wagemaker, Z. Li, S. Ganapathy, Y. Xu, Z. Zhou, M. Sarilar and M. Wagemaker, *Adv Energy Mater*, 2019, **9**, 1900237.

35 L. Chen, Y. Ruan, G. Zhang, Q. Wei, Y. Jiang, T. Xiong, P. He, W. Yang, M. Yan, Q. An and L. Mai, *Chemistry of Materials*, 2019, **31**, 699–706.

36 B. Zhang, J. Chen, W. Sun, Y. Shao, L. Zhang and K. Zhao, *Energies 2022, Vol. 15, Page 4698*, 2022, **15**, 4698.

37 P. Shvets, O. Dikaya, K. Maksimova and A. Goikhman, *Journal of Raman Spectroscopy*, 2019, **50**, 1226–1244.

38 A. Bafaqeer, M. Tahir and N. A. S. Amin, *Appl Surf Sci*, 2018, **435**, 953–962.

39 D. Louloudakis, D. Vernardou, E. Spanakis, M. Suchea, G. Kenanakis, M. Pemble, K. Savvakis, N. Katsarakis, E. Koudoumas and G. Kiriakidis, *Adv Mater Lett*, 2016, **7**, 192–196.

40 K. Guan, K. Duan, G. Yang, L. Tao, H. Zhang, H. Wan, R. Yang, J. Zhang, H. Wang and H. Wang, *Mater Today Adv*, 2022, **14**, 100230.

41 V. Augustyn, J. Come, M. A. Lowe, J. W. Kim, P. L. Taberna, S. H. Tolbert, H. D. Abruña, P. Simon and B. Dunn, *Nature Materials 2013 12:6*, 2013, **12**, 518–522.

42 B. K. Lesel, J. S. Ko, B. Dunn and S. H. Tolbert, *ACS Nano*, 2016, **10**, 7572–7581.

43 J. Gong, H. Li, K. Zhang, Z. Zhang, J. Cao, Z. Shao, C. Tang, S. Fu, Q. Wang and X. Wu, *Nanomaterials*, 2022, **12**, 1438.

Open Access Article. Published on 22 November 2024. Downloaded on 11/26/2024 9:52:47 AM.
This article is licensed under a Creative Commons Attribution-NonCommercial 3.0 Unported Licence.

Journal of Materials Chemistry A Accepted Manuscript

View Article Online
DOI: 10.1039/D4TA06572G

44 Chengyan Cai, Zengren Tao, Yuanfei Zhu, Yuanming Tan, Anding Wang, Haiyun Zhou and Yangyi Yang, *Nanoscale Adv*, 2021, **3**, 3780–3787.

45 S. Roy, S. Marzorati, A. Schievano and D. Pant, *Encyclopedia of Sustainable Technologies*, 2017, 245–259.

46 M. Zhao, Y. Luo, L. Zhu, D. Cai, Y. Zhuang, Q. Chen and H. Zhan, *J Alloys Compd*, 2022, **913**, 165124.

47 Y. Jiang, D. Ba, Y. Li and J. Liu, *Advanced Science*, DOI:10.1002/ADVS.201902795.

48 F. Li, Y. L. Liu, G. G. Wang, D. Yan, G. Z. Li, H. X. Zhao, H. Y. Zhang and H. Y. Yang, *J Mater Chem A Mater*, 2021, **9**, 9675–9684.

49 H. Zhang, J. Wang, Q. Liu, W. He, Z. Lai, X. Zhang, M. Yu, Y. Tong and X. Lu, *Energy Storage Mater*, 2019, **21**, 154–161.

50 J. Liu, C. Guan, C. Zhou, Z. Fan, Q. Ke, G. Zhang, C. Liu, J. J. Wang P Liu, C. Zhou, C. Guan, Z. Fan, Q. Q. Ke, J. Wang, G. Z. Zhang and C. Liu, *Advanced Materials*, 2016, **28**, 8732–8739.

51 K. Fang, F. Li, G. G. Wang, Y. L. Liu, M. L. Tan, D. Q. Zhao, H. Y. Zhang and J. C. Han, *J Mater Sci Technol*, 2023, **143**, 84–92.

52 H. Yang, Y. Wan, K. Sun, M. Zhang, C. Wang, Z. He, Q. Li, N. Wang, Y. Zhang, H. Hu and M. Wu, *Adv Funct Mater*, DOI:10.1002/ADFM.202215076.

Open Access Article. Published on 22 November 2024. Downloaded on 11/26/2024 9:52:47 AM.
This article is licensed under a Creative Commons Attribution-NonCommercial 3.0 Unported Licence.

Journal of Materials Chemistry A Accepted Manuscript

View Article Online
DOI: 10.1039/D4TA06572G

All scientific data has been reported in the main manuscript and supporting information. The raw data files are available upon request from the corresponding authors.

Open Access Article. Published on 22 November 2024. Downloaded on 11/26/2024 9:52:47 AM.
This article is licensed under a Creative Commons Attribution-NonCommercial 3.0 Unported Licence.

Journal of Materials Chemistry A Accepted Manuscript